The role of roughness geometry in frictional wave dissipation

Solène Dealbera, Damien Sous, Denis Morichon, Héloïse Michaud

The role of roughness geometry in frictional wave dissipation

Solène Dealbera[a,*], Damien Sous[a,b], Denis Morichon[a], Héloïse Michaud[c]

[a] *Université de Pau et des Pays de l'Adour, E2S-UPPA, SIAME, Anglet, France*
[b] *Université de Toulon, Aix Marseille Univ, CNRS, IRD, MIO, Marseille, France*
[c] *Shom, Antenne de Toulouse, BP 45017 – 31032 Toulouse, France*

Abstract

Bottom friction dissipation is a key factor for wave attenuation in nearshore environments presenting complex geomorphological structures, such as rocky or coral shores. The present paper reports on a series of laboratory experiments performed in a wave flume with controlled wave conditions and seabed structures. Using the frequency-integrated short-wave analysis and classical models for bottom friction and breaking dissipation, the wave friction factor and the hydraulic roughness parameter were estimated from the experimental data. The former varies from 0.17 to 98 while the latter varies from 0 to 0.291 m. The observations reveal the combined influence of several topographical metrics, including the standard deviation, the skewness, the directionality and the effective slope of the seabed elevation. A metric-based multi-varied model for the hydraulic roughness parameter is proposed and confronted with other field data recovered on coral and rocky shores.

Keywords: Waves, Roughness, Friction, Surf zone, Physical model

1. Introduction

Nearshore areas worldwide combine a growing interest from human societies, leading to continually expanding anthropization, and strong vulnerability to extreme events and climate change effects. Understanding nearshore hydrodynamics remains a major challenge for developing accurate modeling systems able to prevent coastal hazards, such as coastal flooding during extreme events and coastline erosion (Fringer et al., 2019). A strong focal point in nearshore studies is the wave-driven hydrodynamics, playing a key role in circulation, sediment transport and shoreline exposure.

Nearshore area is characterized by shallowing bathymetry that strongly affects wave propagation inducing a series of hydrodynamic processes including shoaling, reflection, refraction,

*Corresponding author: solene.dealbera@univ-pau.fr

depth-induced breaking (Dean and Dalrymple, 1991), non-linear transfers between frequency bands (Hasselmann et al., 1973) and bottom-induced friction dissipation (Madsen, 1995). The contributions of those processes to nearshore wave transformation were mostly investigated for sandy beaches with gently sloping and relatively smooth bottom. However, sandy beaches represent less than 30% of the world's coastlines (Bird, 2000). The remaining nearshore areas are characterized by more complex morphological structures including rough seabeds on rocky or coral shores, steep slopes and/or uneven bathymetry or seagrass canopies. Modeling wave transformation in such environments remains a challenge, due to a more complex physics and often to a lack of detailed in-situ documentation due to access difficulty.

In the presence of large roughness elements, such as rocks and coral pinnacles, bottom friction can be expected to play an important role in wave transformation, potentially dominant over depth-induced breaking in wave attenuation for very rough terrain. In the past few years, field experiments over coral reefs (Lowe et al. (2005a, 2007); Quiroga and Cheung (2013); Monismith et al. (2015); Van Dongeren et al. (2013); Rogers et al. (2016); Sous et al. (2023)) and rocky platforms (Farrell et al. (2009); Ogawa et al. (2015); Poate et al. (2018); Gon et al. (2020); Lavaud et al. (2020)) have provided detailed analysis of frictional wave dissipation over rough seabeds, leading in particular to a series of field estimates of the wave friction factor f_w, identified as a key quantity for bottom friction dissipation. The overall trend is that an increase in roughness results in an increase in f_w. Consequently, classical bottom friction models (Swart, 1974; Soulsby et al., 1993; Madsen, 1995) connect f_w with the ratio of the near-bed wave orbital amplitude A_o to a single length-scale characterizing the roughness, the so-called hydraulic roughness parameter k_r. However, while the existing parameterizations have shown robust performance for high values A_o/k_r, the application of classical bottom friction models in very rough environments remains uncertain. In particular, data are very sparse for $A_o/k_r < 1$ (Nielsen, 1992; Gon et al., 2020)(Simons et al., 2000; Dixen et al., 2008; Sumer and Fuhrman, 2020). In addition, one might expect that in the presence of very large roughness, the relative submergence (ratio between k_r and the local depth D) can become a critical parameter in shallow areas such as surf-zones Davis et al. (2021).

A second unresolved issue is the definition of a clear quantitative connection between frictional processes and geometrical roughness structure. A few studies have simultaneously documented hydrodynamic processes and topographical structure. The recurring trend is that k_r should primarily scale with the standard deviation of fine-scale seabed elevation, both for unidirectional (Aberle et al., 2010; Flack and Schultz, 2014) or wave-driven oscillatory (Lowe et al., 2005a; Sous et al., 2023) flows. However, discrepancies between studies for identical ratios of A_o/k_r (Gon et al., 2020) tend to indicate that other roughness features may be involved in the definition of k_r. Most of the existing insights into the relation between fine bed features and shear stress have been provided by analysis of the rough

turbulent canonical boundary layer (see the recent review of Chung et al. (2021)). A series of roughness metrics have been highlighted to assess the effect of roughness structure height (based on average roughness height or standard deviation of roughness elevation), frontal solidity related to pressure drag exposure, plane solidity (ratio of plan area of roughness elements to total plan area) or spatial arrangements of roughness structures such as clustering, directionality or spatial heterogeneity. Laboratory experiments have provided a few empirical formulas accounting for statistical metrics of bed topography (Chung et al., 2021). However, relevant experimental observations in comparable ranges of metrics remain sparse, mainly due to the cost of performing such parametric studies. Furthermore, note that bed metrics developed for idealized geometries, such as networks of vertical cylinders or cubic elements (Lowe et al., 2005b; Chung et al., 2021), may be barely applicable on real seabeds where the roughness structure presents a fractal dimension with no clear roughness structure spacing and arrangement (Duvall et al. (2019); Stewart et al. (2019); Sous et al. (2020)).

The present laboratory study aims to improve our understanding of frictional wave dissipation in the surf zone for rough seabeds by i) assessing the performance of standard friction parameterizations over a wide range of roughness conditions and ii) proposing quantitative relationships between k_r, the classical frictional length-scale, and a selection of relevant metrics describing the geometrical structure of seabed roughness. In this context, a series of laboratory experiments were carried out considering several roughness layouts to obtain a wave friction database exploring a wide range of A_o/k_r and D/k_r ratios. The first section describes the experimental setup, the data processing, the theoretical models used to extract wave friction parameters and the seabed topographical metrics. The second section presents the results, including the mono- and multi varied statistical models of the hydraulic roughness while the Discussion section summarizes the observations and their limitations and provides prospects for future research works.

2. Methods

2.1. Experimental facility

The experiments were carried out in the CASH (Canal Aéro-Sédimento-Hydrodynamique) wave flume at Seatech engineering school, University of Toulon. The flume is made of glass, 6m long and 0.5m wide, and equipped with a linearly sloping bed of 1/20. A piston wavemaker, with an absorbing system at the back, was used to generate waves on the 1m-long horizontal bottom section before the sloping bed (Figure 1).

2.1.1. Instrumentation

A series of resistive wave gauges were used to measure the free surface elevation over the sloping bed. The wave gauges were deployed along three alignments: a central alignment in

the axis of the channel where 20 wave gauges are distributed every 17 cm, and two secondary alignments as control points, parallel to the central one and placed at 12.5 cm on either side of it, with one wave gauge out of 4 (Figure 1). The acquisition frequency was 100Hz.

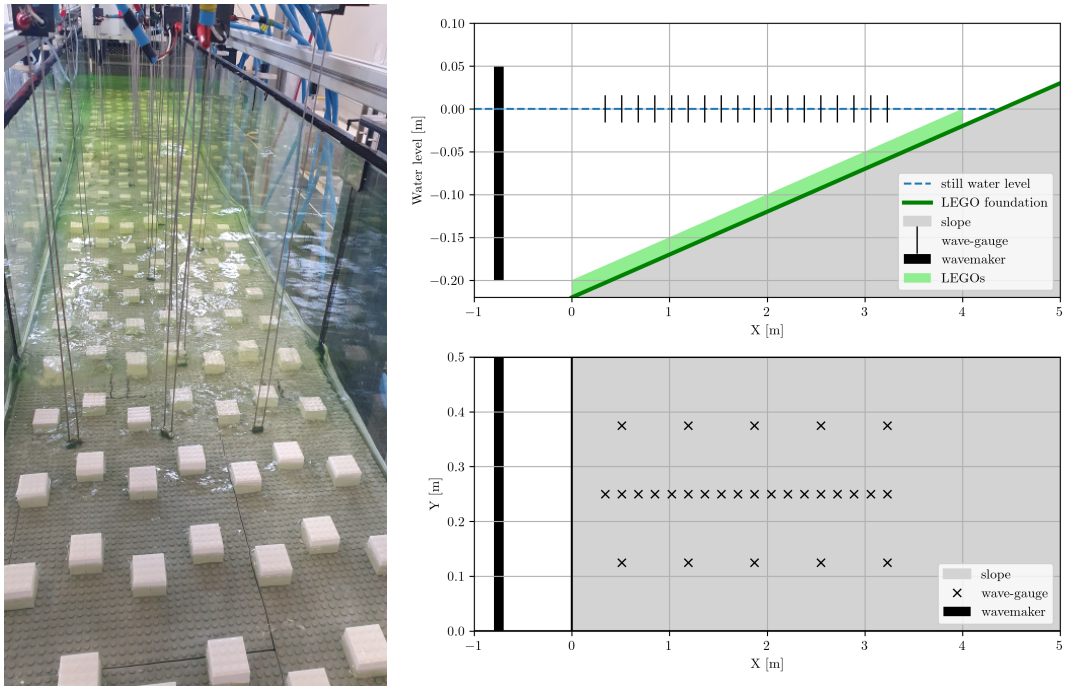

Figure 1: Picture of the TR3 layout and diagram of the wave flume setup and instrumentation.

2.1.2. Wave runs

Each experiment consisted of a 5-min run of irregular waves generated from a JONSWAP spectrum (peak enhancement factor at 7). Wave parameters are summarized in Table 1. The still water depth was kept constant at 0.22m.

Wave run	**Peak period** [s]	**Mean period** [s]	**Significant wave height** [m]	**Iribarren number**
W1	1.0	0.8	0.065	0.089
W2	1.0	0.8	0.075	0.083
W3	1.2	1.0	0.047	0.086
W4	1.2	1.0	0.061	0.075
W5	1.2	1.0	0.071	0.070

Table 1: Wave run parameters.

The Iribarren number is given by the following relationship $\xi = \beta/\sqrt{2\pi H_{s,o} T_{p,o}^2}$, where β is the slope of the seabed, $H_{s,o}$ and $T_{p,o}$ are the measured offshore significant wave height and peak period, corrected for the effect of the shoaling. The Iribarren values range between 0.064 and 0.079 and indicate a spilling breaker (Galvin Jr., 1968), validated by visual observations in the flume.

2.1.3. Wave gauge processing

The spectral density of variance at each gauge was first computed from the free surface elevation time series using a fast Fourier transform. Incident and reflected spectral wave components are then separated using the three-gauge method (Drevard et al., 2009). The incident spectra are then integrated over the short wave (SW) frequency band $\frac{f_p}{2} < f < 3f_p$, where f_p is the peak frequency, to provide H_{rms} the spectral root mean square height of the incident short waves given by the following formula: $H_{rms} = \sqrt{8 \int E(f) df}$, with $E(f)$ the spectral energy density.

2.1.4. Seabed layouts

A series of 27 seabed layouts was tested on the beach slope while the horizontal section of the flume remained untouched. The reference smooth seabed layout, referred to as RF, was made using stainless steel plates. The first rough layout, referred to as BS, was made of LEGO® plastic base plates showing an isotropic distribution of short cylinders of 1mm diameter, 8mm spacing and 1mm height. Twenty-five additional types of beds were created using selected layouts of plastic blocks fixed on the BS seabed. Three main patterns studied were the isotropic quincunx (referenced as QC), the anisotropic brick (referenced as BK) and the trimodal height block (referenced as M3). For each pattern, several configurations (referred to as the *layouts*) of height, width, and spacing were tested. The quincunx layouts were defined by the cubic block height (H) and spacing (SP) while the brick layouts were defined by the cobbled block height (H), length (L - transverse dimension) and spacing (SP), as shown in Figure 2 and described in Table 2. Variations in alignments of the quincunx pattern created new layouts with cross-shore (TR) and along-shore (LG) bars, by changing either the transversal shift (LX) or longitudinal shift (LY), their height (H), length (L) and streamwise dimension (P). As for the trimodal pattern, two layouts were arranged, one with a quincunx pattern with varying heights and one with random groups of different height blocks. Figure 3 displays an illustrative series of layouts. Statistical topographical features for each layout are described in Section 2.5 and listed in Appendix A.

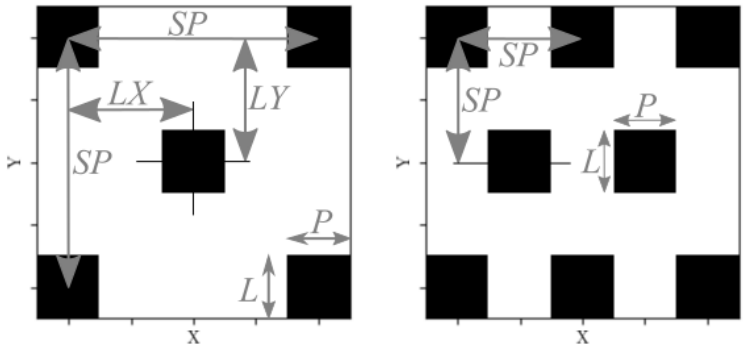

Figure 2: Main seabed patterns: quincunx on the left and brick on the right. Parameters definition are based on waves coming from the left side.

Layout	**H**	**L**	**P**	**SP**	**LX**	**LY**
Layout name	*Height [m]*	*Length [m]*	*Streamwise dimension [m]*	*Spacing between block lines [m]*	*Transversal shift between block lines [m]*	*Longitudinal shift between block lines [m]*
RF	0	0	0	-	-	-
BS	0.001	0.001	0.001	-	0.008	0.008
QC1	0.016	0.016	0.016	0.032	0.016	0.016
QC2	0.016	0.016	0.016	0.064	0.032	0.032
QC3	0.032	0.032	0.032	0.064	0.032	0.032
QC4	0.032	0.032	0.032	0.128	0.064	0.064
QC5	0.048	0.048	0.048	0.096	0.048	0.048
QC6	0.048	0.048	0.048	0.192	0.096	0.096
QC7	0.048	0.048	0.048	0.288	0.144	0.144
QC8	0.064	0.064	0.064	0.256	0.128	0.128
QC9	0.064	0.064	0.064	0.512	0.256	0.256
LG1	0.032	0.032	0.032	0.128	0.064	0.000
LG2	0.032	0.032	0.032	0.128	0.064	0.032
LG3	0.048	0.048	0.144	0.288	0.192	0.144
LG4	0.048	0.048	0.048	0.192	0.096	0.000
LG5	0.048	0.048	0.048	0.192	0.096	0.048
TR1	0.032	0.480	0.032	0.256	-	-
TR2	0.032	0.032	0.032	0.128	0.000	0.064
TR3	0.032	0.032	0.032	0.128	0.032	0.064
TR4	0.048	0.480	0.048	0.384	-	-
TR5	0.048	0.144	0.048	0.384	0.192	0.192
TR6	0.048	0.048	0.048	0.192	0.000	0.096
TR7	0.048	0.048	0.048	0.192	0.048	0.096
BK1	0.064	0.032	0.032	0.096	-	-
BK2	0.032	0.096	0.096	0.128	-	-
M3A	0.016 - 0.032 - 0.048	0.032	0.032	0.128	0.064	0.064
M3B	0.016 - 0.032 - 0.048	0.032	~ 0.096	-	-	-

Table 2: Seabed layout parameters

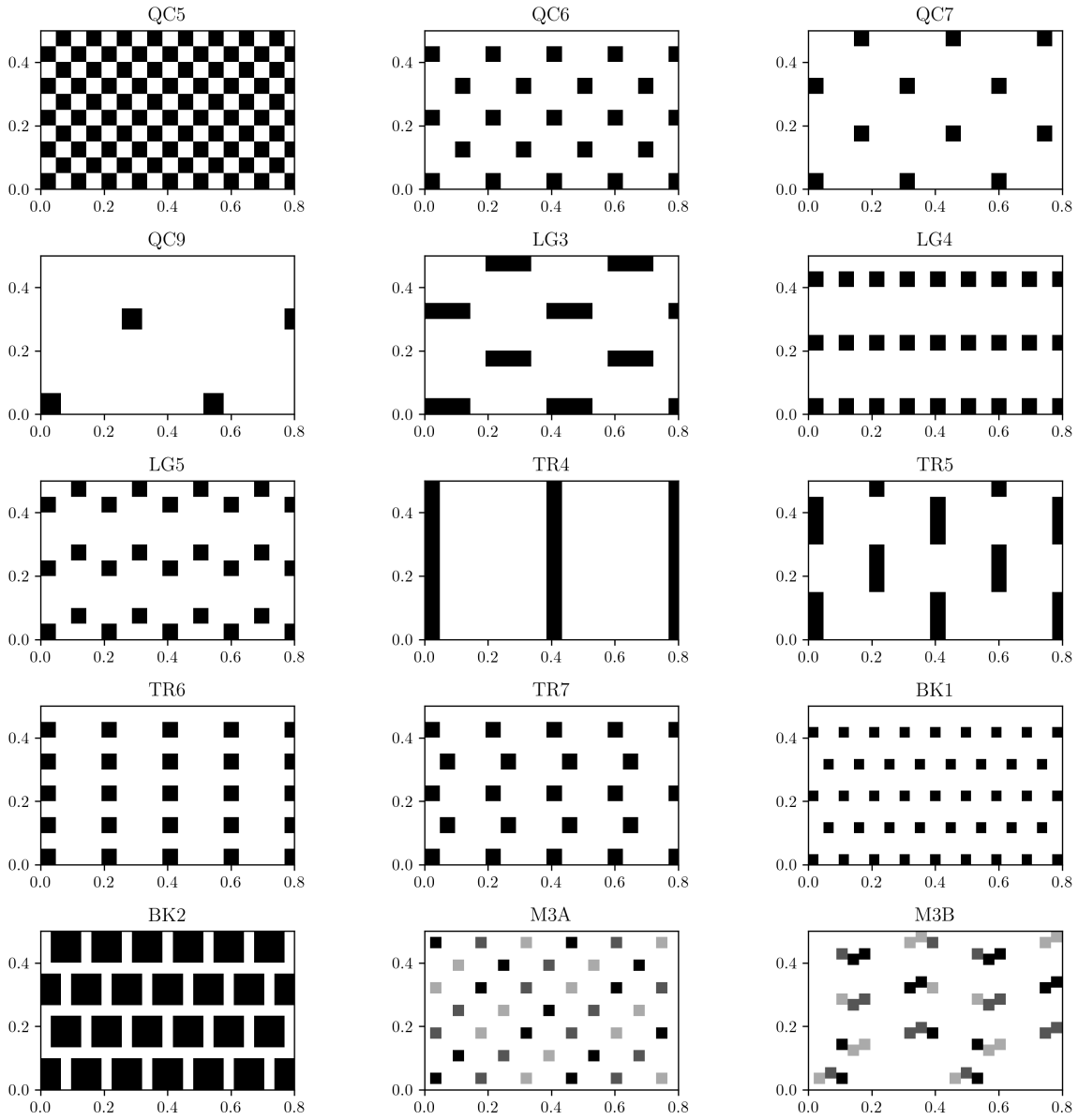

Figure 3: Plane view examples of seabed layouts. x- and y-axes correspond to cross- and along-shore directions. Waves come from the left side. Grey color levels for M3A end M3B indicated the different bloc heights.

2.2. Performance estimators

Two classical estimators are used hereafter to quantify the accuracy of the agreement between observations and model predictions: the normalized root mean square error (NRMSE) based on the normalization of the root mean square error (RMSE) and the Willmott index (WI) which shows a standardized error measure between 0 and 1:

$$RMSE = \sqrt{\frac{1}{n}\sum_{i}^{n}\left(\hat{\Theta}_i - \Theta_i\right)^2} \tag{1}$$

$$NRMSE = \frac{RMSE}{\sqrt{\frac{1}{n}\sum_{i}^{n}\Theta_i^2}} \times 100 \tag{2}$$

$$WI = 1 - \frac{\sum_{i}^{n}\left(\hat{\Theta}_i - \Theta_i\right)^2}{\sum_{i}^{n}\left(\left|\hat{\Theta}_i - \overline{\Theta}\right| + \left|\Theta_i - \overline{\Theta}\right|\right)^2} \tag{3}$$

where n is the number of values, $\hat{\Theta}$ is the prediction value, Θ the observed value and $\overline{\Theta}$ the mean of observed values.

2.3. Determination of wave dissipation contributions

The present section describes the implementation of a simple wave energy model used to process the experimental observations. The aim is to compare the combined contributions of wave breaking and bottom friction with the total measured dissipation, allowing to extract wave frictional parameters from the measurements, namely the wave friction factor and the hydraulic roughness.

2.3.1. Energy flux balance

We consider unidirectional wave propagation along a reference cross-shore x-axis, addressed in a frequency-integrated approach over the SW band. When averaged over many wave cycles, the wave energy flux balance in the absence of mean current can be written as:

$$\frac{\partial EC_g}{\partial x} = \overline{\varepsilon_t} \tag{4}$$

where E is the wave energy, C_g the wave group velocity and $\overline{\varepsilon_t}$ is the total wave-averaged dissipation. E and C_g are estimated by the linear theory formulations for irregular waves:

$$E = \frac{\rho g}{8} H_{rms}^2 \tag{5}$$

with ρ as the density of the water and g the acceleration of gravity and

$$C_g = \frac{1}{2}\left(1 + \frac{2kD}{\sinh(2kD)}\right)\frac{\omega}{k} \tag{6}$$

where k and ω are the wave number and the angular frequency associated with the peak period and D the water depth, using the dispersion relationship $\omega^2 = gk\tanh(kD)$.

$\overline{\varepsilon_t}$ combines the effect of breaking dissipation $\overline{\varepsilon_b}$ and frictional dissipation $\overline{\varepsilon_f}$:

$$\overline{\varepsilon_t} = \overline{\varepsilon_b} + \overline{\varepsilon_f} \tag{7}$$

$\overline{\varepsilon_t}$ is calculated at each wave gauge using a centered scheme with the two neighbouring gauges, for each wave case and each seabed layout.

Following previous experiments in the same CASH wave flume (Sous et al., 2021), frictional dissipation over smooth surfaces is negligible, i.e. we neglect sidewall friction for rough cases and sidewall and bottom friction for smooth RF case. A bi-spectral analysis has been performed on a smooth representative case, using RF layout and W2 wave conditions, to estimate the non-linear energy between SW and IG bands. The process has been detailed in Appendix C. It has showed a weak effect of non-linear energy transfer on the estimation of friction factor and we expect them to play an even weaker role in shallow rough environments.

2.3.2. Breaking-induced dissipation

The standard wave model of Thornton and Guza (1983) (Eq. 24, hereinafter named TG83) is used to estimate breaking-induced dissipation $\overline{\varepsilon_b}$:

$$\overline{\varepsilon_b} = \frac{B^3}{4}\rho g\frac{f_p}{D}\int_0^\infty H^3 p(H)\left(\frac{H_{rms}}{\gamma D}\right)^n\left[1 - \exp\left(-\left(\frac{H}{\gamma D}\right)^2\right)\right]dH \tag{8}$$

where B is a breaking coefficient, $p(H)$ the probability density function of the crest-to-trough wave height H, γ a breaking parameter and n a constant coefficient taking at 2, following TG83. The model parameters γ and B and the wave height distribution $p(H)$ are optimized against the smooth RF reference seabed layout for each wave run. γ is first estimated from the linear fit of the H_{rms}/D ratio relationship obtained from the inner surf zone measurements. The second adjustable parameter B is optimised by minimising the NRMSE and maximising the WI by comparing the measured and modelled dissipation. The γ and B parameter pair is estimated for each wave case on the smooth RF seabed and assumed to be constant for all other seabed layouts. The final γ values are 0.36, 0.45, 0.30, 0.40 and 0.45 for W1 to W5 cases, respectively, while the B values are 0.57, 0.66, 0.63, 0.70 and 0.73 for W1 to W5 cases, respectively.

To model $p(H)$, we use a modified Rayleigh distribution to take into account the statistics observed in our flume, with a stronger weight of high waves in the surf zone:

$$p(H) = \frac{2H}{H_{rms}^2} \exp\left[-\left(\frac{H - H_0/4}{H_{rms}}\right)^2\right] \tag{9}$$

where H_0 is the spectral root mean square of incident waves measured at the offshore wave gauge. Figure 4 displays comparisons of cross-shore profiles of wave height and energy flux dissipation between measurements, standard TG83 model, with same values of γ and the following optimized values of B for each wave run: 0.80, 0.83, 0.86, 0.97 and 1.03, and distribution-adjusted TG83 model. The improvements provided by the adjusted distribution in the TG83 model are straightforward for both wave height and energy flux dissipation.

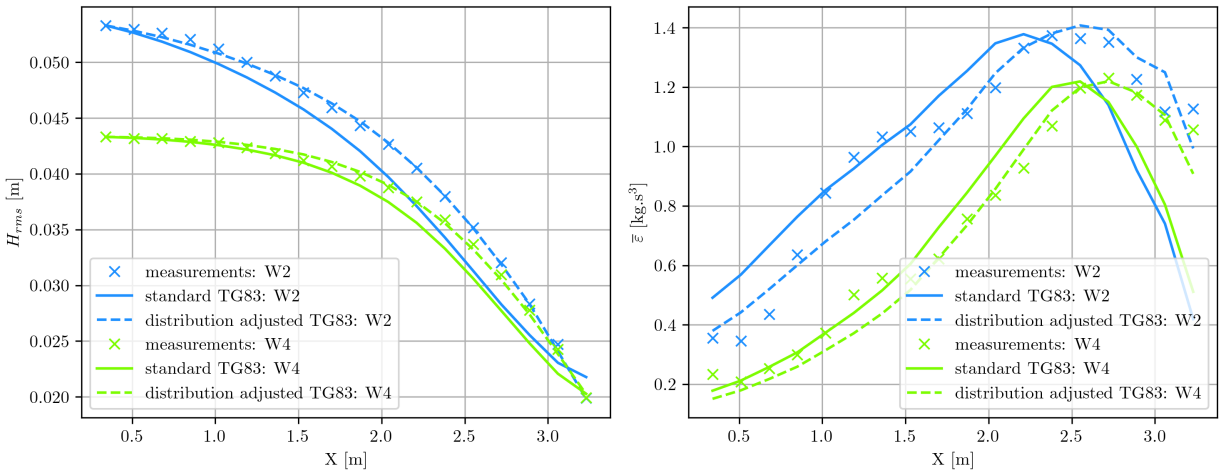

Figure 4: Cross-shore profiles of H_{rms} (left pannel) and $\overline{\varepsilon_t}$ (right pannel). Laboratory measurements are depicted by cross symbols while standard and distribution adjusted TG83 model are presented in solid and dashed lines, respectively. Green and blue colors correspond to W2 and W4 cases.

2.3.3. Frictional dissipation

The SW-integrated bottom friction dissipation model is again based on the seminal work of TG83:

$$\overline{\varepsilon_f} = \frac{\rho f_w}{4\sqrt{\pi}} \left(\frac{\pi H_{rms}}{T_{m01} \sinh kD}\right)^3 \tag{10}$$

where T_{m01} is the average wave period and k the wave number associated with T_{m01}.

Following Swart (1974); Madsen et al. (1988); Nielsen (1992), the wave friction factor f_w is related to the ratio of the wave orbital excursion at the bottom to a typical vertical

roughness scale, the so-called hydraulic roughness parameter k_r (or equivalent Nikuradse roughness height), through the following expression:

$$f_w = \exp\left(a_1 \left(\frac{A_o}{k_r}\right)^{a_2} + a_3\right) \tag{11}$$

where a_1, a_2 and a_3 are dimensionless empirical constants taken as 5.0, -0.15 and -5.9 (Sous et al., 2023) and $A_o = u_o/\omega$ the bottom orbital excursion with u_o the bottom orbital velocity given by the linear theory:

$$u_o = \frac{\pi H_{rms}}{T_{m01} \sinh kD} \tag{12}$$

2.4. Extraction of wave frictional parameters

For each wave run and rough seabed layout, the measured total dissipation can be compared to the combined contributions of breaking and frictional dissipation to infer two governing frictional parameters from the measurements: the wave friction factor and the hydraulic roughness.

2.4.1. Wave friction factor

The wave friction factor f_w is directly estimated from experimental data combining Equations 7 and 10:

$$f_w = 4\sqrt{\pi}\left(\frac{\overline{\varepsilon_t} - \overline{\varepsilon_b}}{\rho}\right)\left(\frac{T_{m01} \sinh kD}{\pi H_{rms}}\right)^3 \tag{13}$$

where $\overline{\varepsilon_t}$ is deduced from the experimental estimations of energy flux gradient using Equation 4 and $\overline{\varepsilon_b}$ from the calibrated breaking model.

2.4.2. Dissipation-optimized hydraulic roughness

The wave energy flux model from Equation 4, combining the breaking dissipation from Equation 8 and the frictional dissipation from Equation 10, is used to predict the cross-shore evolution of H_{rms}. The sole free parameter is k_r, the hydraulic roughness, which is used as a fitting parameter to obtain the best agreement with the measured H_{rms} profile. The optimization is performed by minimising the NRMSE and maximising the WI, limiting the analysis to $H_{rms} > 0.01\,m$ data. Therefore, for each wave run and rough seabed layout, a single optimized value of the hydraulic roughness parameter $k_{r,o}$ is obtained.

2.5. Topographical metrics

The rough seabed topography is described for all layouts by a Digital Elevation Model (DEM) depicting the 2D seabed elevation $\aleph(x, y)$, where y is the coordinate along the longshore direction, with a 0.008m definition (see e.g. Figure 3). For all rough seabed layouts,

statistical properties were calculated, focusing on statistical metrics remaining workable on non-idealized topography: $\sigma_{\aleph}$ the standard deviation of seabed elevation, $Sk_{\aleph}$ the skewness, $\Delta_{\aleph}$ the directionality and $ES_{\aleph,x}$ the cross-shore effective slope. The former two statistical moments are computed on the full 2D DEM matrix, classically defined as:

$$\sigma_{\aleph} = \sqrt{\frac{1}{n}\sum_{i}^{n}\left(\aleph_i - \overline{\aleph}\right)^2} \tag{14}$$

$$Sk_{\aleph} = \frac{\frac{1}{n}\sum_{i}^{n}\left(\aleph_i - \overline{\aleph}\right)^3}{\left[\frac{1}{n}\sum_{i}^{n}\left(\aleph_i - \overline{\aleph}\right)^2\right]^{3/2}} \tag{15}$$

where $\overline{\aleph}$ is the seabed elevation mean defined as $\overline{\aleph} = \frac{1}{n}\sum_{i}^{n}\aleph_i$. The directionality estimator $\Delta_{\aleph}$ is based on the computation of directional standard deviations $\sigma_{\aleph,x}$ and $\sigma_{\aleph,y}$, in cross-shore and along-shore directions, respectively:

$$\Delta_{\aleph} = \frac{\overline{\sigma_{\aleph,x}} - \overline{\sigma_{\aleph,y}}}{\overline{\sigma_{\aleph,x}} + \overline{\sigma_{\aleph,y}}} \tag{16}$$

$\Delta_{\aleph}$ is equal to zero for a fully isotropic roughness structure and tends to -1/1 for increasingly anisotropic layouts with along-shore/cross-shore uniform roughness structure, respectively.

The alongshore-averaged cross-shore effective slope (Napoli et al., 2008; Chung et al., 2021), which is a measure of the frontal solidity, is estimated as:

$$ES_{\aleph,x} = \frac{1}{L_x}\overline{\sum\left|\frac{\partial\aleph(x)}{\partial x}\right|} \tag{17}$$

with L_x is the cross-shore length and $\aleph(x)$ is the seabed elevation in the cross-shore direction.

2.6. Procedure summary

The overall data analysis procedure is summarized in Figure 5. In addition to the steps described above, a multi-variate regression (MVR) is used to build a predictive model for hydraulic roughness, see Section 3.5.

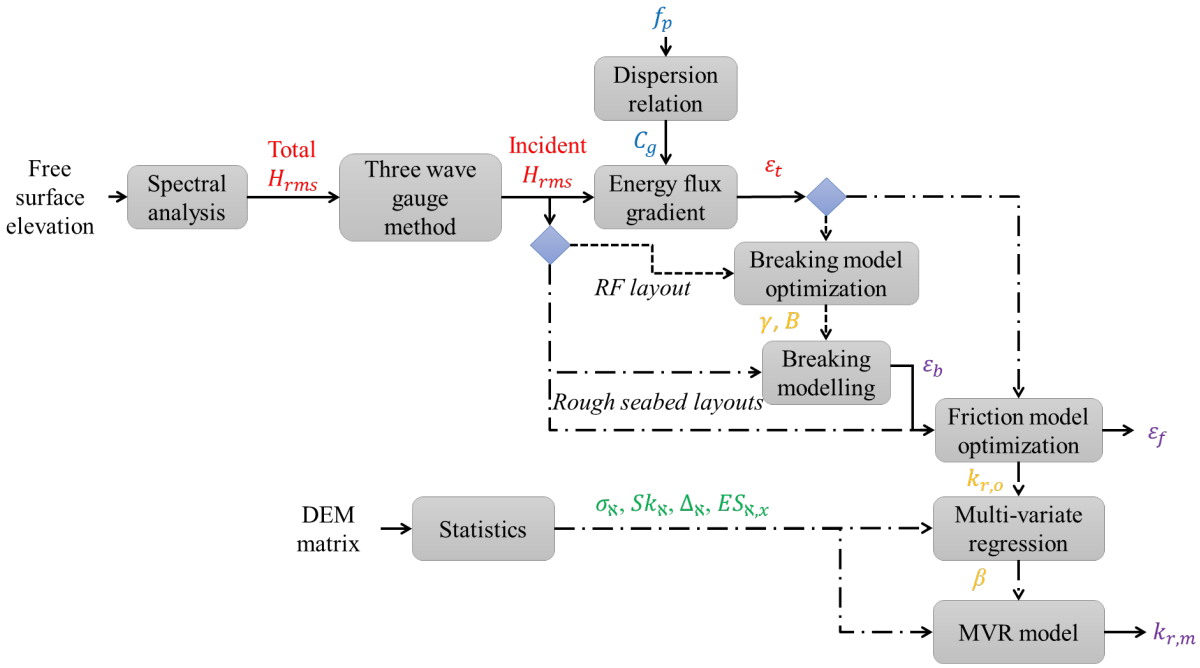

Figure 5: Method summary: wave parameters are shown in blue, seabed geometry statistics in green, measured values in red, optimized values in orange and modelled values in purple.

3. Results

3.1. Illustrative cases

Figure 6 depicts, for wave case W3 (see Table 1), the cross-shore H_{rms} profiles for four different seabed layouts: RF, QC4, TR1 and QC6. The smooth RF profile (black line) shows a first nearly constant section in the wave propagation and then a decrease due to the overwhelming effect of wave breaking starting around $X = 2\,m$. For rough seabeds, the first main trend is an enhancement of wave dissipation with σ_N. Comparing for instance RF, QC4 and QC6 with $\sigma_N = 0$, 0.011 and 0.016 m, respectively, we observe both stronger dissipation rate and earlier inception of dissipation across the profile, even far offshore from the breaking point for the rougher case. However, σ_N is not the only controlling factor of frictional dissipation. This is demonstrated by TR1, which has a smaller σ_N (0.012) than QC6 but a stronger wave attenuation, with different Δ_N values (respectively 1 and 0).

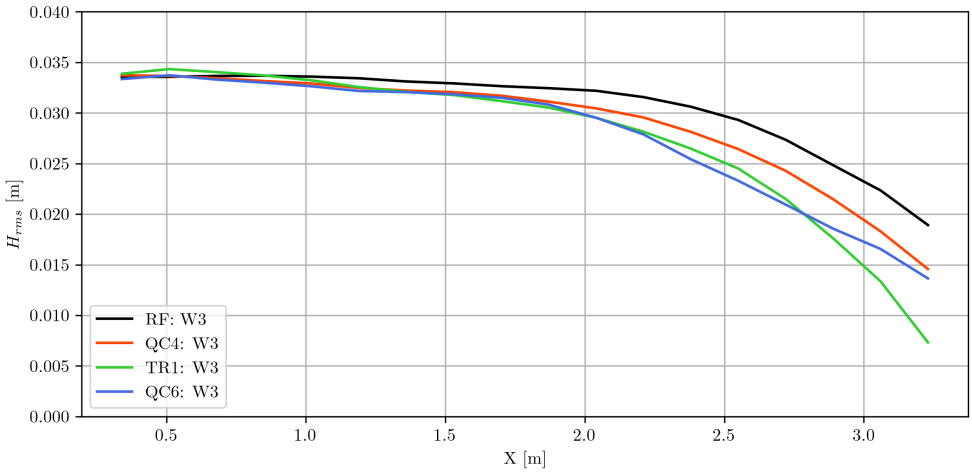

Figure 6: Cross-shore profile for H_{rms} for three seabed layouts : RF (black), QC4 (red), TR1 (green) and QC6 (blue). QC4 and TR1 have the same $\sigma_{\aleph} = 0.011$ and QC4 and QC6 have the same $\Delta_{\aleph} = 0$. Profiles are shown for the W3 wave run.

3.2. Wave friction factor vs monoscale hydraulic roughness

Figure 7 depicts the relationship between the experimental wave friction factor f_w (Eq. 13) and A_o/k_r ratio. It is first assumed here that $k_r = k_r^{\sigma_{\aleph}}$, a monoscale function only depending on $\sigma_{\aleph}$: $k_r^{\sigma_{\aleph}} = 6\sigma_{\aleph}$. The experimental f_w are bin-averaged over logarithmically-spaced A_o/k_r bins, while the color levels depict the different seabed layouts. An additional comparison is made with the prediction of the theoretical formulation from Equation 11.

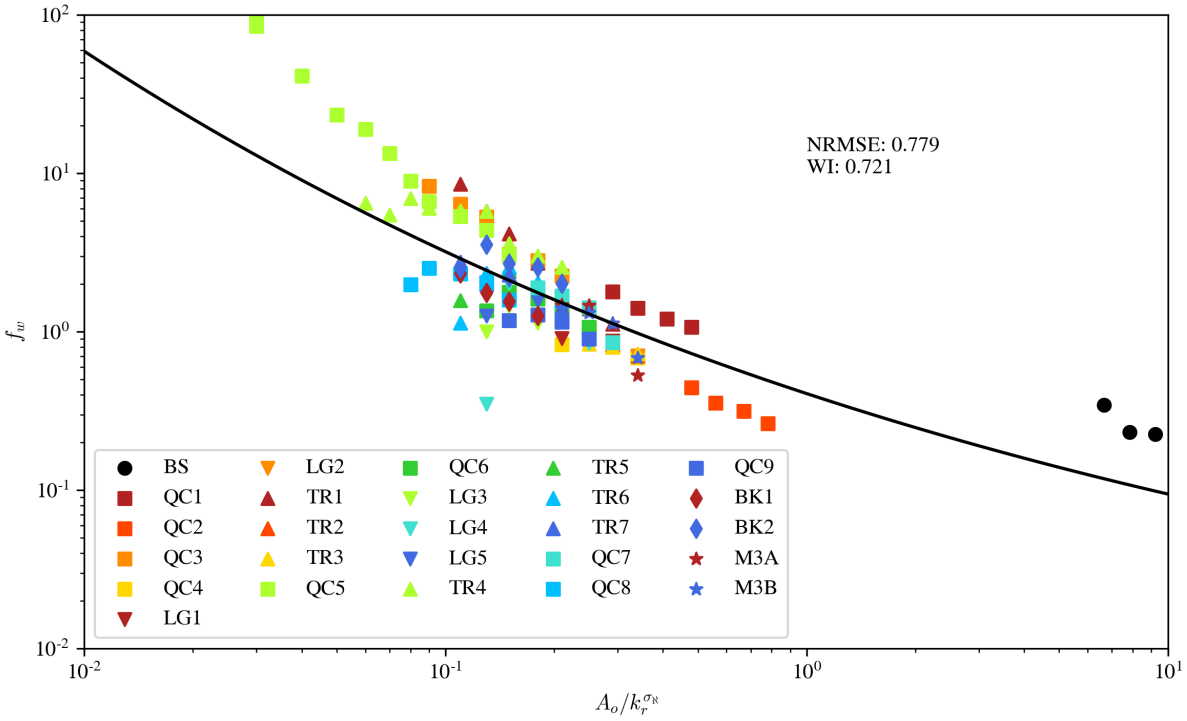

Figure 7: Bin-averaged values of measured f_w plotted as a function of $A_o/k_r^{\sigma_\aleph}$ colored by seabed layouts, where $k_r^{\sigma_\aleph}$ is the hydraulic roughness modelled using a monoscale relation as $k_r^{\sigma_\aleph} = 6\sigma_\aleph$. The solid black line represents Madsen's prediction Madsen (1995) (Equation 11) using Sous et al's parameterization Sous et al. (2023).

The experimental bin-averaged friction factor ranges from 0.17 to 98. The overall trend of the f_w data shows the expected behavior, i.e. a decrease of friction for increasing A_o/k_r ratio. For the purpose of comparison with other datasets, the range of A_o/k_r covered by the present experiments corresponds to $0.15 < A_o/\sigma_\aleph < 30.90$, i.e. in the typical range of rough bed friction studies documented in the field Lowe et al. (2005a); Gon et al. (2020); Poate et al. (2018); Sous et al. (2023). The experimental f_w shows a reasonable overall agreement with the friction model prediction (NRMSE=0.779, WI=0.721). However, a visible spread is observed between the different seabed layouts with a factor more than 5 for f_w obtained at similar A_o/k_r. Following the previous observations on H_{rms} profiles in Figure 6, it is expected that at least part of the observed discrepancies are due to the variation in roughness structure, suggesting that the standard deviation may not be the sole scaling of hydraulic roughness. The first qualitative analysis can be inferred from a closer look at Figure 7. The plane solidity effect can be assessed by comparing cases QC6 and BK2, the latter showing a much lower

skewness than the former (2.26 vs -0.4). Low-skewness BK2 shows overall higher f_w than QC6, which tends to indicate that higher plane solidity is associated with higher friction, at least in the documented range. Roughness directionality shows a significant effect on wave friction factor. Comparing for instance QC6 with LG4, LG5, TR4 and TR5, one notes that longitudinal/transverse alignments produce a decrease/increase of friction for the same statistical moments. The only effect of effective slope, related to frontal solidity, is poorly identified with direct observations in Figure 7.

3.3. Dissipation-optimized $k_{r,o}$

The calculation of dissipation-optimized roughness height described in Section 2.4.2 provides $k_{r,o}$ values ranging from 0 m to 0.291 m. As expected the lowest values are observed for the smoothest layouts (BS and QC2) while the largest values $k_{r,o} > 0.2\,m$ are obtained for the highest $\sigma_\aleph$ layout (QC5), including the extreme 0.291m value associated with the most energetic wave run W2.

In order to gain further insight into the potential multi-varied nature of hydraulic roughness, Figure 8 depicts scatterplots of the dissipation-optimized $k_{r,o}$ versus $\sigma_\aleph$, indicating the different wave cases as color levels. The previous conclusion is confirmed: a strong dependence between $k_{r,o}$ and $\sigma_\aleph$, indicating that $\sigma_\aleph$ is a key parameter in the formulation of the background friction parameterization. However, for identical values of $\sigma_\aleph$, a noticeable variability of $k_{r,o}$ is shown, meaning other metrics should be involved in the bottom friction parameterization.

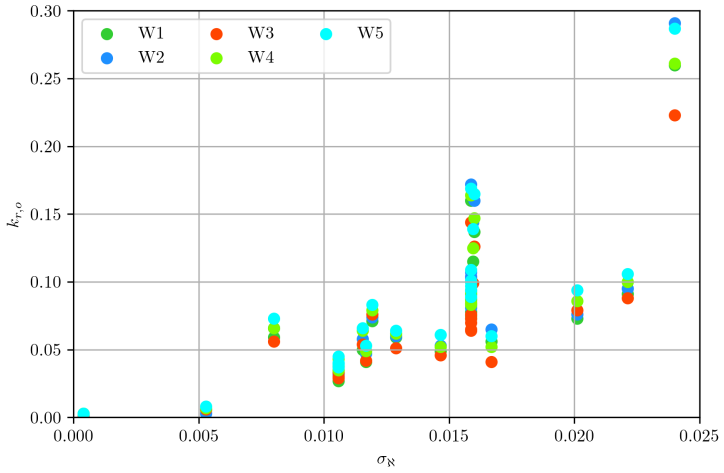

Figure 8: Scatterplots of $k_{r,o}$ versus $\sigma_\aleph$ colored wave cases.

3.4. Performance of the standard friction parameterization in high roughness environment

Further tests are carried out on the dissipation-optimized hydraulic roughness to assess the limitations of the standard friction parameterization given by Equation 11. Once the optimized hydraulic roughness $k_{r,o}$ has been obtained for each seabed and each wave run, a series of tests is performed comparing the agreement between the measured H_{rms} profile and the modeled H_{rms} computed from the energy flux balance (Eq. 4) including breaking dissipation given by Equation 8 and frictional dissipation from Equation 10 based on $k_{r,o}$. We first test the agreement between experiments and model against the $A_o/\sigma_{\aleph}$ ratio, in order to explore the potential degradation of the predictive capacities for large relative roughness height. The best results are obtained for $A_o/\sigma_{\aleph} > 2.5$, with NRMSE lower than 4 % and WI higher than 0.995. A degradation of the performance is observed for smaller values of $A_o/\sigma_{\aleph}$ but the accuracy remains correct, with median NRMSE and WI of about 5 % and 0.99, respectively. The model prediction capacity does not further degrade for the lowest values of $A_o/\sigma_{\aleph}$.

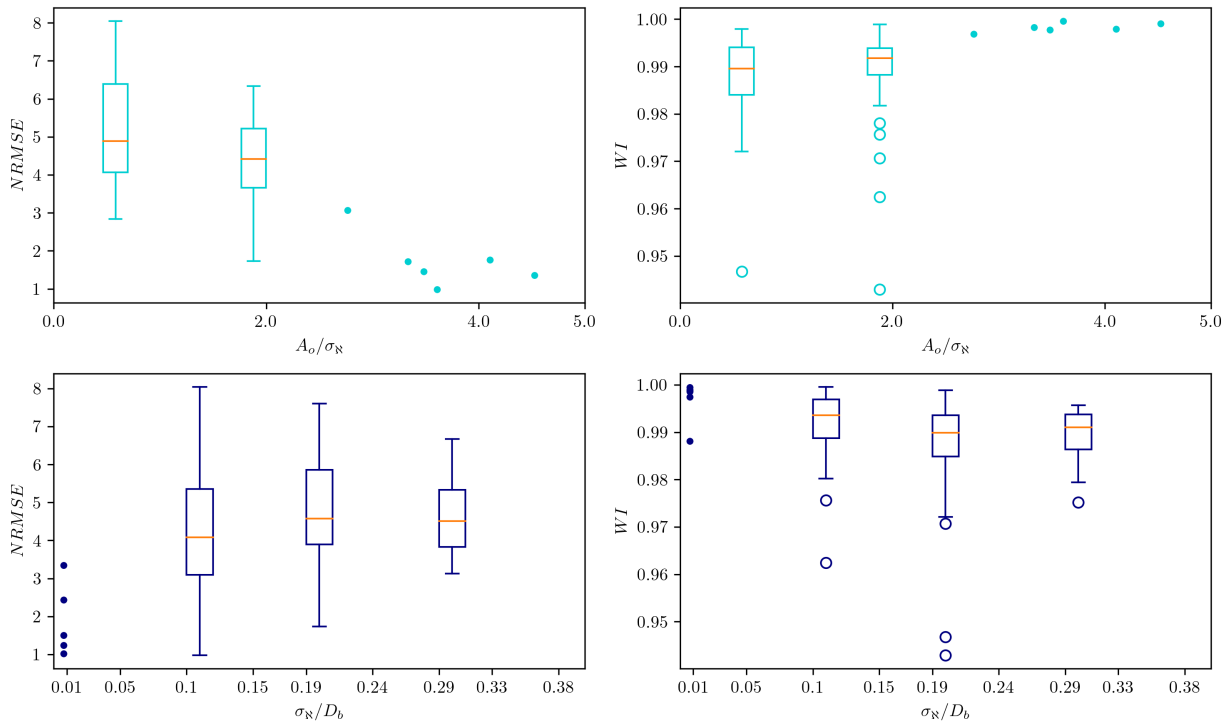

Figure 9: Plot and binned boxplots of NRMSE and WI versus $A_o/\sigma_\aleph$ for the following intervals : [0.30,0.80,1.30,2.00] (in cyan) and $\sigma_\aleph/D_b$ for the following intervals : [0.00,0.30,0.70] (in blue). The central red line is the median, the edges of the box are the 25 and 75-th percentiles, the whiskers extends to 1.5 of the interquartile range while the outliers are plotted individually as circles. Single points are individual datapoints.

A second series of tests is performed on the relative roughness submergence ratio. This being variable across the profile, the breaking point value $\sigma_\aleph/D_b$ is used, where D_b is the breaking depth obtained at $H_{rms}/D_b \approx 0.7$ (Symonds et al., 1995). The first observation is that, similarly to the previous results, best wave model prediction performances are observed at low submergence ratio ($\sigma_\aleph/D_b < 0.1$) with NRMSE and WI remaining mostly lower than 4 % and higher than 0.990, respectively. A degradation of the accuracy is observed for $\sigma_\aleph/D_b > 0.1$ but the performance remains rather stable and does not strongly drop for high submergence ratio. Most of the poor-accuracy outliers are again related to the W3 wave run, without any straightforward explanation.

3.5. Multi-varied hydraulic roughness model

Based on the previous observations, a multi-varied analysis is carried out to connect the optimized hydraulic roughness $k_{r,o}$ to the topography metrics and then provide a pre-

dictive model for hydraulic roughness. The most important controlling factor for frictional dissipation is the seabed elevation standard deviation, as expected from several decades of observations (e.g. Swart (1974); Nielsen (1992); Madsen (1995); Lowe et al. (2005a); Sous et al. (2023)), among others. A linear dependency is first assumed here, following Lowe et al. (2005a); Sous et al. (2023). The effect of skewness, identified for instance by comparing cases QC6 and BK2 in Figure 7, is observed to be non-linear, maybe related to regime changes of the boundary layer (Flack et al., 2020). Over the studied range of skewness, the best fit has been obtained using a tanh-based relationship. Power-law formulations, such as those used in steady boundary layer studies Flack and Schultz (2010); Flack et al. (2020), do not provide clear improvement. The effects of directionality and effective slope are both taken into account using a simple linear relationship. Finally, we propose the following hydraulic roughness model:

$$k_{r,m} = 4\sigma_{\aleph} \left(1 + \beta_s + \beta_d + \beta_e\right) \tag{18}$$

where respectively β_s, β_d and β_e are the adjusted parameterizations for respectively $Sk_{\aleph}$, $\Delta_{\aleph}$ and $ES_{\aleph,x}$ given by:

$$\beta_s = -0.3 \left(\tanh\left(Sk_{\aleph} - 0.8\right) - 1\right) \tag{19}$$

$$\beta_d = \Delta_{\aleph} \tag{20}$$

$$\beta_e = 1.1 ES_{\aleph,x} \tag{21}$$

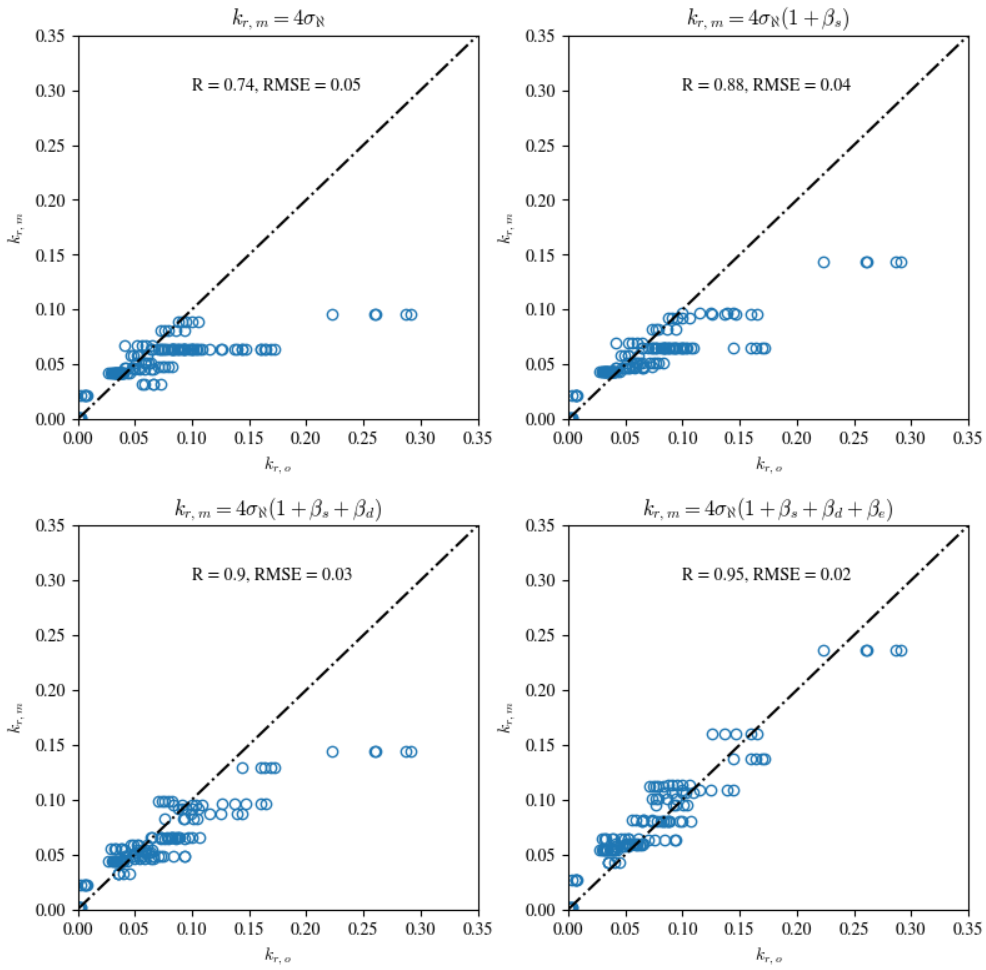

Figure 10: Plots of multi-variate modelled $k_{r,m}$. Values for $k_{r,m}$ and $k_{r,o}$ are given in Appendix B.

The experimental wave friction factor f_w is plotted against the $A_o/k_{r,m}$ to assess the improvement brought by the consideration of additional topography statistical metrics in the definition of the hydraulic roughness. The results displayed in Figure 11 show an overall better collapse of the data than for the mono-varied model from Figure 7. The agreement with the friction model is also clearly improved, with significantly decreased NRMSE and increased WI values.

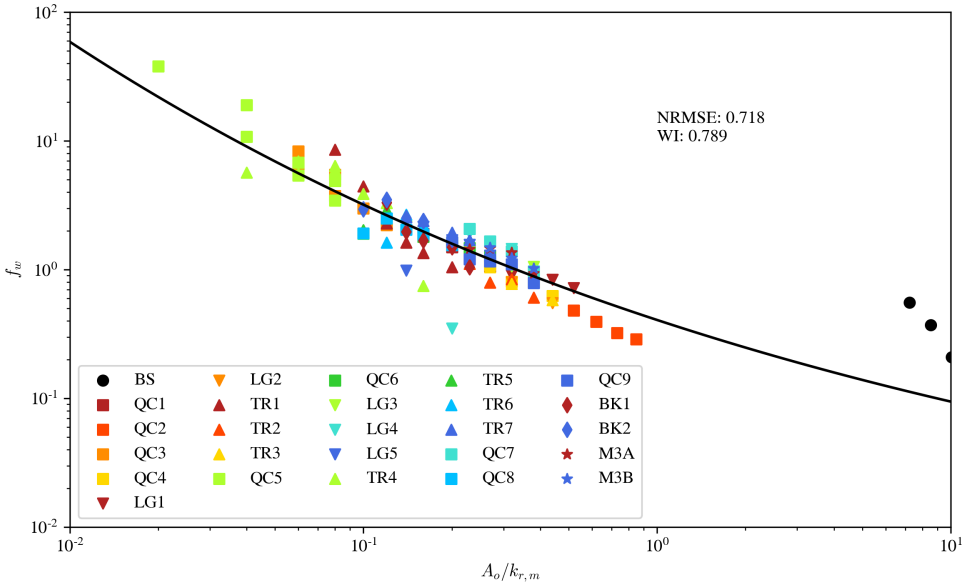

Figure 11: Bin-averaged values of measured f_w plotted as a function of $A_o/k_{r,m}$ colored by seabed layouts. The solid black line represents Madsen's prediction Madsen (1995) (Equation 11) using Sous et al's parameterization Sous et al. (2023).

4. Discussion

The present study aimed to compare novel laboratory data on wave attenuation by frictional dissipation over rough seabeds with standard wave friction models. The first observation is that the linear wave model, including classical breaking and friction parameterization, shows satisfactory predictive capability even for the larger roughness layout studied here, related to small orbital amplitude to roughness ratio and large relative submergence ratio. A slight degradation is observed when increasing roughness height, but the performance remains overall stable. These observations tend to support the use of traditional wave boundary layer theory for parameterizing friction, even when the actual roughness height exceeds the initial framework assumptions Madsen (1995). This indicates furthermore that the prediction errors associated with standard wave models would not be able to fully explain the difference in wave friction factors observed between sites (Gon et al., 2020; Sous et al., 2023).

The observed variability of f_w is certainly largely controlled by the dynamics of the interactions between coherent structures and topography. One may for instance expect that the larger space between roughness elements will allow the development of larger coherent structures, which can explain the observed relationship between topography skewness and friction factor. However, the 3D structure of most layouts combined with the oscillating forcing and

the breaking-induced turbulence should strongly complicate the coherent vortex patterns. Current instrumentation does not allow us to detail these interactions, and developing new measurement methods coupled with 3D Navier-Stokes modelling will be a required step to enhance the understanding of the internal flow dynamics.

Based on an optimisation of the modeled cross-shore wave height evolution against experimental data, the hydraulic roughness is estimated for each type of roughness and connected to a series of topographical metrics to provide a multi-varied model for hydraulic roughness. For the sake of interpretability, the statistical model proposed here assumes simple relationships between topography metrics and hydraulic roughness. While this approach provides useful new insights into the hydraulic roughness for wave studies, more complex dependencies may likely be involved. A variety of correlation formulations have been proposed in the case of canonical boundary layer cases (Flack and Schultz, 2010; Barros et al., 2018; Forooghi et al., 2017; Flack et al., 2020) but their direct application to the present wave friction study have not provided improved performance. The further improvement of the k_r model will require a much denser experimental plan, combining laboratory data on more realistic terrain together with real-scale field data at the required resolution, with regard to both hydrodynamic and topographical aspects. Here, experimental constraints fixed the seabed slope value at 1/20, which is considered as very steep in regard to most studied sites where it does not go below 1/30 (Poate et al., 2018), except for the Banneg island rocky cliff sites documented by Dodet et al. (2018). It is difficult to estimate *a priori* the effect of such a slope on friction processes without having access to fine documentation of turbulent processes close to the seabed. Further experiments will have to be carried out on flat seabed and gentle slopes to identify and discard any potential slope effect. Furthermore, the peak enhancement factor was kept constant at 7 for wave-maker control constraints. The role of spectrum shape on dissipative processes will merit further exploration, although there is generally good consistency between full spectral approaches (Madsen, 1995; Sous et al., 2023; Lowe et al., 2005a) and frequency-integrated approaches (Gon et al., 2020) in terms of friction factor.

The roughness metrics assessed in the present paper have been selected for their simplicity, making them generalizable for other laboratory and in-situ configurations. However, it is worthwhile mentioning that a number of other metrics have been proposed (Chung et al., 2021), with potential complex interdependencies. The role of roughness directionality has been accounted for using a simple metric and a linear parameterization in the k_r model, providing a clear improvement when compared to the model which ignores directionality. However, two cases with partial streamwise alignments (LG4 and LG5) are still poorly described by the model, with a lower friction factor than predicted. Further improvements are needed, both in metric definition and parameterization in the k_r model to improve the description of directionality in such configurations. The effects of higher-order statistical moments, such as kurtosis, could not have been explored independently by the present experiments due to

a strong correlation with the skewness. The spatial heterogeneity of roughness appeared to play a role by reducing the friction factor for increasing heterogeneity. This can be observed by comparing cases QC4 and M3A in Figure 7, the former/latter showing regular/irregular roughness height distribution, respectively, for the same $\sigma_{\aleph}$. The regular distribution (QC4) shows generally higher friction factors than the irregular one (M3A). However, no unequivocal metric of spatial heterogeneity has been found when applied to the present seabed layout, but its effect is likely accounted for, at least partly, by the metrics selected for the multi-varied hydraulic roughness model. It has also been hypothesized that different spatial clustering scales may have led to stronger impacts on frictional dissipation (Sarakinos and Busse, 2019; Chung et al., 2021). The effect of roughness clustering appeared to be weak for the tested configurations. This is highlighted by the comparison of M3A and M3B layouts in Figure 7, which show very close values of f_w despite a widely different spatial arrangement, M3B being much more clustered than M3A for similar other properties.

The comparison of the proposed k_r model with field estimates is not straightforward, mainly due to the lack of documentation of the fine topographical statistics of the studied field sites. A first view is given in Figure 12 which depicts the wave friction factor against A_o/k_r for the present data (averaged over wave cases) and a selected set of field observations from Lowe et al. (2005a); Lentz et al. (2016); Poate et al. (2018); Gon et al. (2020). For the latter field data points, the seabed standard elevations have been provided by the authors while we attribute arbitrary, but a priori realistic, values for skewness, directionality and effective slope taken at 0.5, 0 and 0.15, respectively. These taken values are based on a comparative study of 9 rocky and coral sites (Sous et al., 2024). The overall agreement is satisfactory both in terms of the trend in A_o/k_r dependency and order of magnitude, indicating that both the laboratory data and the statistical k_r model proposed here can be used as guidelines for predictions of wave frictional dissipation. Discrepancies between the observations and the model remain, which calls for further adjustments of the model and emphasizes the need for further laboratory experiments to explore more realistic seabed structures, together with site-comparative in-situ surveys allowing to identify the differentiating metrics between field sites. The values obtained here remain sensitive to the choice of topographical parameters. The comprehensive testing of the present parameterization requires, for each test site, a combined survey of hydrodynamics and fine topography, which remains very rare in the existing published data but should be planned in further studies, where possible. Studies carried out by Simons et al. (2000); Dixen et al. (2008); Sumer and Fuhrman (2020) propose that the friction factor can be modelled proportionally to $\left(\frac{A_o}{k_r}\right)^{-1}$ for small values of $\frac{A_o}{k_r}$. Attempt to fit this model to our data points is pictured Figure 12 with an optimized value of 0.3.

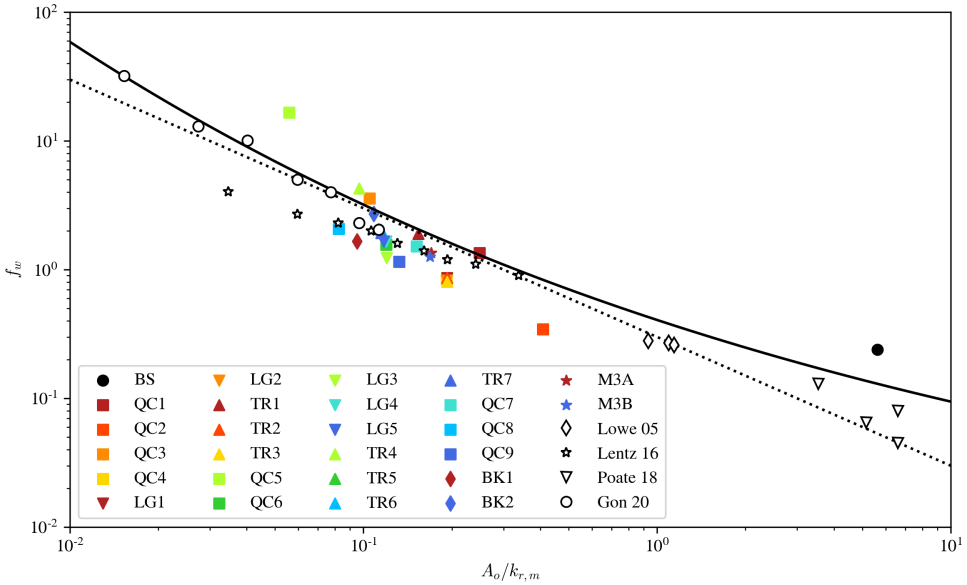

Figure 12: Seabed layout averaged values of measured f_w plotted as a function of $A_o/k_{r,m}$ colored by seabed layouts. Empty-filled black symbols represent field data from previous studies (Lowe et al. (2005a); Lentz et al. (2016); Poate et al. (2018); Gon et al. (2020)) plotted against $A_o/k_{r,m}$ using typical values for $Sk_{\aleph} = 0.5$,$\Delta = 0$ and $ES_{\aleph,x} = 0.15$. The solid black line represents Madsen's prediction Madsen (1995) (Equation 11) using Sous et al's parameterization Sous et al. (2023).The dotted black line represents the $0.3(A_o/k_{r,m})^{-1}$ prediction of (Dixen et al., 2008).

Note finally that the definition of the bathymetry remains an important and challenging issue when attempting to build unified parameterization from observations at various sites. The bathymetry is generally reconstructed from topographical surveys using low-pass filters or rolling averaging techniques. Using different approaches will lead to different definitions of depth, which remains a key parameter of the wave action balance. The present study, based on the reference smooth layout, should provide comparable depth referential to the moving-window 10-th percentile approach used by Sous et al. (2023) but may lead to differences for f_w estimates inferred with other frameworks.

5. Conclusion

Bottom friction caused by the boundary layer is known to be a dominant factor in coastal areas with complex bathymetry. Conventional integrated approach models for small roughness have been developed to estimate the friction coefficient and remain in use within their range of validity. The aim of this study was to produce a database of wave friction in a controlled environment to study the impact of roughness structure on frictional dissipation.

The presence of roughness elements impeding the flow induces a general offshore shift of the inflexion point in the cross-shore profile of root mean square wave height. Optimization of the friction model using hydraulic roughness shows that despite the wide range of wave-induced conditions in the surf zone, the model predictions remain robust, although degraded for weakly submerged flows. Wave attenuation was shown to be not only strongly controlled by the standard deviation of the bottom elevation but also by other bottom characteristics, which were identified as the frontal porosity via the effective slope and skewness, and as the arrangement of roughness structures via the directionality. As the effective slope increases, the coefficient of friction increases. The more the arrangements form bars in the direction of wave propagation (longitudinal), the more the coefficient decreases and conversely for the case of perpendicular bars (transverse). With a multi-variate regression, a simple relationship connecting these metrics to hydraulic roughness was established and significantly improves the results of the friction model. The comparison of the hydraulic roughness model with the results of previous studies suggests that further analysis is needed to explore the effects of the roughness structure metrics on frictional dissipation and to improve this model before confrontation with relevant field measurements and implementation in spectral models.

Acknowledgements

The authors acknowledge the assistance of V. Rey in providing a scientific contribution to reflection component processing.

Appendix A: Table of seabed layout parameters

Seabed layout name	**Block height**	$\sigma_{\aleph}$	$Sk_{\aleph}$	$\Delta_{\aleph}$	$ES_{\aleph,x}$
RF	0.000	0.000	0.000	0.000	0.000
BS	0.001	0.000	1.626	0.000	123.647
QC1	0.016	0.008	0.000	0.000	119.792
QC2	0.016	0.005	2.268	0.000	29.948
QC3	0.032	0.016	0.000	0.000	114.583
QC4	0.032	0.011	2.268	0.000	28.646
QC5	0.048	0.024	0.000	0.000	109.375
QC6	0.048	0.016	2.268	0.000	27.344
QC7	0.048	0.013	3.144	0.000	15.625
QC8	0.064	0.022	2.088	0.000	27.778
QC9	0.064	0.015	3.881	0.000	10.417
LG1	0.032	0.011	2.268	-0.268	28.646
LG2	0.032	0.011	2.268	0.000	28.646
LG3	0.048	0.017	2.068	-0.224	7.813
LG4	0.048	0.016	2.268	-0.268	27.344
LG5	0.048	0.016	2.268	0.000	27.344
TR1	0.032	0.012	1.789	1.000	31.250
TR2	0.032	0.011	2.268	0.268	26.042
TR3	0.032	0.011	2.268	0.000	28.646
TR4	0.048	0.016	2.268	1.000	15.625
TR5	0.048	0.016	2.268	0.464	21.484
TR6	0.048	0.016	2.268	0.268	23.438
TR7	0.048	0.016	2.268	0.000	27.344
BK1	0.064	0.020	2.475	-0.225	52.083
BK2	0.032	0.016	-0.167	-0.153	39.062
M3A	0.016 & 0.032 & 0.048	0.012	2.910	0.000	16.927
M3B	0.016 & 0.032 & 0.048	0.012	2.955	0.023	11.393

Table .3: Seabed layout metrics.

Appendix B: Table of optimized and modelled hydraulic roughness

Wave run	**W1**	**W2**	**W3**	**W4**	**W5**	
Seabed layout name			$k_{r,o}$ [m]			$k_{r,m}$ [m]
BS	0.002	0.001	0.000	0.003	0.003	0.002
QC1	0.059	0.066	0.056	0.066	0.073	0.082
QC2	0.006	0.003	0.006	0.007	0.008	0.027
QC3	0.137	0.160	0.126	0.147	0.165	0.160
QC4	0.034	0.039	0.037	0.043	0.040	0.054
QC5	0.260	0.291	0.223	0.261	0.287	0.236
QC6	0.073	0.083	0.064	0.083	0.089	0.081
QC7	0.059	0.060	0.051	0.062	0.064	0.059
QC8	0.091	0.095	0.088	0.100	0.106	0.114
QC9	0.049	0.053	0.046	0.052	0.061	0.064
LG1	0.035	0.040	0.035	0.035	0.045	0.043
LG2	0.033	0.032	0.033	0.038	0.037	0.054
LG3	0.056	0.065	0.041	0.052	0.060	0.064
LG4	0.075	0.093	0.070	0.084	0.094	0.059
LG5	0.078	0.081	0.065	0.085	0.097	0.081
TR1	0.071	0.074	0.076	0.079	0.083	0.112
TR2	0.033	0.032	0.029	0.038	0.039	0.065
TR3	0.027	0.031	0.030	0.038	0.040	0.054
TR4	0.160	0.172	0.144	0.164	0.169	0.138
TR5	0.091	0.103	0.084	0.100	0.109	0.107
TR6	0.094	0.104	0.076	0.092	0.101	0.096
TR7	0.087	0.107	0.073	0.088	0.100	0.081
BK1	0.073	0.076	0.079	0.086	0.094	0.101
BK2	0.115	0.144	0.099	0.125	0.139	0.109
M3A	0.050	0.058	0.054	0.064	0.066	0.060
M3B	0.041	0.047	0.042	0.049	0.053	0.058

Table .4: Optimized $k_{r,o}$ and MVR modelled $k_{r,m}$ values.

Appendix C: Non-linear energy transfers

The assumption is made that non-linear energy transfers can be neglected in our SW-frequency-integrated energy flux balance. An estimation of the so-called S_{nl} term has been performed on a smooth representative case, using RF layout and W2 wave conditions. As the relative contribution of non-linear transfers to the energy balance is expected to decrease with increasing rough due to a growing importance of frictional dissipation, the smooth bed is considered as the worst case scenario in terms on non-linear transfers.

The method used here is to compare the measured SW-integrated flux gradient with S_{nl}. The former is estimated between successive sensor pairs along the beach profile using Equations 4, 5 and 6. The latter is the spatially-averaged and SW-frequency-averaged triad source term $\langle S_{nl} \rangle$. First, at each sensor, the spectral nonlinear transfers of energy between triads of frequencies $S_{nl,j}$ (j denotes the frequency component) are modelled with the Boussinesq theory of Herbers et al. (2000) over the full wave spectrum, assuming that the wave field is weakly nonlinear, weakly dispersive, and that these effects are of similar order (Herbers and Burton, 1997; Martins et al., 2021):

$$S_{nl,j} = \rho g \frac{3\pi f}{D} \sum_{m=-\infty}^{m=\infty} \Im \left\{ B^*_{m,j-m} \right\} \tag{.1}$$

where B is the bispectrum of the free surface elevation computed after Kim and Powers (1979), $\Im\{\cdot\}$ refers to the imaginary part and $*$ denotes the complex conjugate. $S_{nl,j}$ is then frequency-integrated over the SW band. Finally, $\langle S_{nl} \rangle$ approximated as the spatial average of its values at the adjacent sensors using the method of Sous et al. (2023).

Figure .13 depicts the results of the S_{nl} analysis for the REF/W2 experiment. Excepted an adjustment phase close to the wave maker, the estimated flux gradient remains negative with a maximum magnitude reached within the surf zone, in agreement with the observations performed on the SW profile. $\langle S_{nl} \rangle$ remains very weak portion of the wave energy flux gradient, with a local peak contribution lower than 11% of the wave energy balance but generally lower than 1 %. This observation confirms the validity of a negligible influence of non-linear energy transfers in the present experimental configuration.

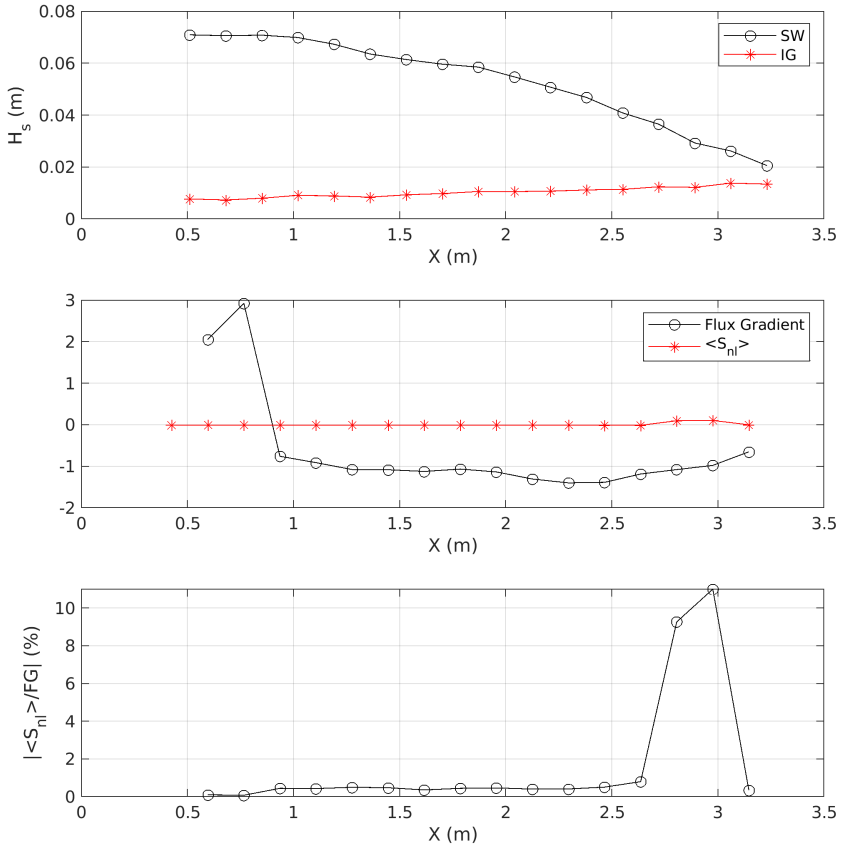

Figure .13: Non-linear transfers for the REF/W2 experiment. Top: compared wave height profiles in the SW (black circles) and IF (red stars) bands. Middle: compared cross-shore profiles of measured wave energy flux gradient and spatially-averaged and SW-frequency-averaged triad source term $\langle S_{nl} \rangle$. Bottom: ratio between $\langle S_{nl} \rangle$ and the wave energy flux gradient.

References

Aberle, J., Nikora, V., Henning, M., Ettmer, B., Hentschel, B., 2010. Statistical characterization of bed roughness due to bed forms: A field study in the Elbe River at Aken, Germany. Water Resources Research 46. URL: http://doi.wiley.com/10.1029/2008WR007406, doi:10.1029/2008WR007406.

Barros, J.M., Schultz, M.P., Flack, K.A., 2018. Measurements of skin-friction of system-

atically generated surface roughness. International Journal of Heat and Fluid Flow 72, 1–7.

Bird, E., 2000. Coastal geomorphology: An introduction. Chichester: John Wiley and Sons.

Chung, D., Hutchins, N., Schultz, M.P., Flack, K.A., 2021. Predicting the drag of rough surfaces. Annual Review of Fluid Mechanics 53, 439–471.

Davis, K.A., Pawlak, G., Monismith, S.G., 2021. Turbulence and coral reefs. Annual review of marine science 13, 343–373.

Dean, R., Dalrymple, R., 1991. Water Wave Mechanics for Engineers and Scientists. volume 2. World Scientific.

Dixen, M., Hatipoglu, F., Sumer, B.M., Fredsøe, J., 2008. Wave boundary layer over a stone-covered bed. Coastal Engineering 55, 1–20. doi:https://doi.org/10.1016/j.coastaleng.2007.06.005.

Dodet, G., Leckler, F., Sous, D., Ardhuin, F., Filipot, J., Suanez, S., 2018. Wave Runup Over Steep Rocky Cliffs. Journal of Geophysical Research: Oceans 123, 7185–7205. doi:10.1029/2018JC013967.

Drevard, D., Rey, V., Fraunié, P., 2009. Partially standing wave measurement in the presence of steady current by use of coincident velocity and/or pressure data. Coastal Engineering 56, 992–1001. doi:10.1016/j.coastaleng.2009.06.002.

Duvall, M.S., Hench, J.L., Rosman, J.H., 2019. Collapsing Complexity: Quantifying Multiscale Properties of Reef Topography. Journal of Geophysical Research: Oceans 124, 5021–5038. doi:10.1029/2018JC014859.

Farrell, E.J., Granja, H., Cappietti, L., Ellis, J.T., Li, B., Sherman, D.J., 2009. Wave transformation across a rock platform, belinho, portugal. Journal of Coastal Research , 5.

Flack, K., Schultz, M., Barros, J., 2020. Skin friction measurements of systematically-varied roughness: probing the role of roughness amplitude and skewness. Flow, Turbulence and Combustion 104, 317–329.

Flack, K.A., Schultz, M.P., 2010. Review of hydraulic roughness scales in the fully rough regime. Journal of fluids engineering 132.

Flack, K.A., Schultz, M.P., 2014. Roughness effects on wall-bounded turbulent flows. Physics of Fluids 26, 101305. doi:10.1063/1.4896280.

Forooghi, P., Stroh, A., Magagnato, F., Jakirlić, S., Frohnapfel, B., 2017. Toward a universal roughness correlation. Journal of Fluids Engineering 139.

Fringer, O.B., Dawson, C.N., He, R., Ralston, D.K., Zhang, Y.J., 2019. The future of coastal and estuarine modeling: Findings from a workshop. Ocean Modelling 143, 101458.

Galvin Jr., C.J., 1968. Breaker type classification on three laboratory beaches. Journal of Geophysical Research 73, 3651–3659. doi:https://doi.org/10.1029/JB073i012p03651.

Gon, C.J., MacMahan, J.H., Thornton, E.B., Denny, M., 2020. Wave dissipation by bottom friction on the inner shelf of a rocky shore. Journal of Geophysical Research: Oceans 125. doi:10.1029/2019JC015963.

Hasselmann, K.F., Barnett, T.P., Bouws, E., Carlson, H., Cartwright, D.E., Eake, K., Euring, J., Gicnapp, A., Hasselmann, D., Kruseman, P., et al., 1973. Measurements of wind-wave growth and swell decay during the joint north sea wave project (jonswap). Ergaenzungsheft zur Deutschen Hydrographischen Zeitschrift, Reihe A .

Herbers, T.H.C., Burton, M.C., 1997. Nonlinear shoaling of directionally spread waves on a beach. Journal of Geophysical Research: Oceans 102, 21101–21114. doi:10.1029/97JC01581.

Herbers, T.H.C., Russnogle, N.R., Elgar, S., 2000. Spectral energy balance of breaking waves within the surf zone. Journal of Physical Oceanography 30, 2723–2737.

Kim, Y.C., Powers, E.J., 1979. Digital Bispectral Analysis and Its Applications to Nonlinear Wave Interactions. IEEE Transactions on Plasma Science 7, 120–131. doi:10.1109/TPS.1979.4317207.

Lavaud, L., Pezerat, M., Coulombier, T., Bertin, X., Martins, K., 2020. Hydrodynamics on a rocky shore under moderate-energy wave conditions. Journal of Coastal Research 95, 1473. doi:10.2112/SI95-284.1.

Lentz, S., Churchill, J., Davis, K., Farrar, J., 2016. Surface gravity wave transformation across a platform coral reef in the r ed s ea. Journal of Geophysical Research: Oceans 121, 693–705.

Lowe, R.J., Falter, J.L., Bandet, M.D., Pawlak, G., Atkinson, M.J., Monismith, S.G., Koseff, J.R., 2005a. Spectral wave dissipation over a barrier reef. Journal of Geophysical Research 110, C04001. doi:10.1029/2004JC002711.

Lowe, R.J., Falter, J.L., Koseff, J.R., Monismith, S.G., Atkinson, M.J., 2007. Spectral wave flow attenuation within submerged canopies: Implications for wave energy dissipation. Journal of Geophysical Research 112, C05018. doi:10.1029/2006JC003605.

Lowe, R.J., Koseff, J.R., Monismith, S.G., 2005b. Oscillatory flow through submerged canopies: 1. velocity structure. Journal of Geophysical Research 110, C10016. doi:10.1029/2004JC002788.

Madsen, O.S., 1995. Spectral wave-current bottom boundary layer flows, in: Coastal Engineering 1994, American Society of Civil Engineers. pp. 384–398. doi:10.1061/9780784400890.030.

Madsen, O.S., Poon, Y.K., Graber, H.C., 1988. Spectral wave attenuation by bottom friction: Theory. Coastal Engineering Proceedings 1, 34. doi:10.9753/icce.v21.34.

Martins, K., Bonneton, P., Michallet, H., 2021. Dispersive characteristics of non-linear waves propagating and breaking over a mildly sloping laboratory beach. Coastal Engineering 167, 103917. doi:10.1016/j.coastaleng.2021.103917.

Monismith, S.G., Rogers, J.S., Koweek, D., Dunbar, R.B., 2015. Frictional wave dissipation on a remarkably rough reef. Geophysical Research Letters 42, 4063–4071. doi:10.1002/2015GL063804.

Napoli, E., Armenio, V., De Marchis, M., 2008. The effect of the slope of irregularly distributed roughness elements on turbulent wall-bounded flows. Journal of Fluid Mechanics 613, 385–394.

Nielsen, P., 1992. Coastal Bottom Boundary Layers and Sediment Transport. volume 4 of *Advanced Series on Ocean Engineering*. WORLD SCIENTIFIC. doi:10.1142/1269.

Ogawa, H., Dickson, M.E., Kench, P.S., 2015. Hydrodynamic constraints and storm wave characteristics on a sub-horizontal shore platform. Earth Surface Processes and Landforms 40, 65–77. doi:10.1002/esp.3619.

Poate, T., Masselink, G., Austin, M.J., Dickson, M., McCall, R., 2018. The role of bed roughness in wave transformation across sloping rock shore platforms. Journal of Geophysical Research: Earth Surface 123, 97–123. doi:10.1002/2017JF004277.

Quiroga, P.D., Cheung, K.F., 2013. Laboratory study of solitary-wave transformation over bed-form roughness on fringing reefs. Coastal Engineering 80, 35–48. doi:10.1016/j.coastaleng.2013.05.002.

Rogers, J.S., Monismith, S.G., Koweek, D.A., Dunbar, R.B., 2016. Wave dynamics of a pacific atoll with high frictional effects. Journal of Geophysical Research: Oceans 121, 350–367. doi:10.1002/2015JC011170.

Sarakinos, S., Busse, A., 2019. Influence of spatial distribution of roughness elements on turbulent flow past a biofouled surface, in: Proceedings of the 11th International Symposium on Turbulence and Shear Flow Phenomena. doi:http://www.tsfp-conference.org/proceedings/2019/238.pdf.

Simons, R., Myrhaug, D., Thais, L., Chapalain, G., Holmedal, L.E., MacIver, R., 2000. Bed Friction in Combined Wave-Current Flows. pp. 216–226. doi:10.1061/40549(276)17.

Soulsby, R., Hamm, L., Klopman, G., Myrhaug, D., Simons, R., Thomas, G., 1993. Wave-current interaction within and outside the bottom boundary layer. Coastal Engineering 21, 41–69. doi:10.1016/0378-3839(93)90045-A.

Sous, D., Bouchette, F., Doerflinger, E., Meulé, S., Certain, R., Toulemonde, G., Dubarbier, B., Salvat, B., 2020. On the small-scale fractal geometrical structure of a living coral reef barrier. Earth Surface Processes and Landforms 45, 3042–3054. URL: https://onlinelibrary.wiley.com/doi/10.1002/esp.4950, doi:10.1002/esp.4950.

Sous, D., Forsberg, P.L., Touboul, J., Nogueira, G.G., 2021. Laboratory experiments of surf zone dynamics under on-and offshore wind conditions. Coastal Engineering 163, 103797.

Sous, D., Martins, K., Tissier, M., Bouchette, F., Meulé, S., 2023. Spectral wave dissipation over a roughness-varying barrier reef. Geophysical Research Letters doi:10.1029/2022GL102104.

Sous, D., Meulé, S., Dealbera, S., Michaud, H., Gassier, G., Pezerat, M., Bouchette, F., 2024. Quantifying the topographical structure of rough seabeds. Submitted to PlosOne .

Stewart, M.T., Cameron, S.M., Nikora, V.I., Zampiron, A., Marusic, I., 2019. Hydraulic resistance in open-channel flows over self-affine rough beds. Journal of Hydraulic Research 57, 183–196. doi:10.1080/00221686.2018.1473296.

Sumer, B.M., Fuhrman, D.R., 2020. Turbulence in Coastal and Civil Engineering. WORLD SCIENTIFIC. doi:10.1142/10829.

Swart, D.H., 1974. Offshore sediment transport and equilibrium beach profiles.

Symonds, G., Black, K.P., Young, I.R., 1995. Wave-driven flow over shallow reefs. Journal of Geophysical Research 100, 2639. doi:10.1029/94JC02736.

Thornton, E.B., Guza, R.T., 1983. Transformation of wave height distribution. Journal of Geophysical Research 88, 5925. doi:10.1029/JC088iC10p05925.

Van Dongeren, A., Lowe, R., Pomeroy, A., Trang, D.M., Roelvink, D., Symonds, G., Ranasinghe, R., 2013. Numerical modeling of low-frequency wave dynamics over a fringing coral reef. Coastal Engineering 73, 178–190. doi:10.1016/j.coastaleng.2012.11.004.